physica status solidi a
www.pss-a.com

Low-Temperature Operation of High-Efficiency Germanium Quantum Dot Photodetectors in the Visible and Near Infrared

Stylianos Siontas, Dongfang Li, Pei Liu, Sartaj Aujla, Alexander Zaslavsky, and Domenico Pacifici*

The temperature-dependent operation of high efficiency Ge quantum dot (QD) photodetectors (PDs) is reported, that shows spectral responsivity of 1.2 A W^{-1}, internal quantum efficiency (IQE) of 228% and signal-to-noise ratio (SNR) equal to 7×10^6 at a wavelength of 640 nm for 12 μW of incident power. The performance of these photodetectors can be improved by reducing the operating temperature, especially at low incident power. For instance, at 10 nW of 640 nm illumination power, lowering temperature from 300 to 100 K improves SNR from 2×10^4 to 2×10^5 and specific detectivity D^* from 1.2×10^{11} to 2×10^{13} cm $Hz^{1/2}$ W^{-1}. This enhanced performance is attributed to saturation of the charging process within the QD layer, that leads to longer hole lifetimes and IQE exceeding 22 000%. Also, the near-infrared performance of these PDs is reported, finding that below 200 K there is a significant near-IR photocurrent (three orders of magnitude larger than the dark current at 1100 nm and two orders of magnitude larger than the dark current at 1300–1550 nm, where only the Ge QDs contribute to optical absorption), leading to operational PDs, albeit at lower D^*.

1. Introduction

High-responsivity, low-noise CMOS-compatible photodetectors (PDs) are required for applications such as optical interconnects on silicon chips and for imaging sensors. Crystalline Ge is compatible with the Si fabrication technology and is characterized by lower synthesis temperatures, a larger absorption coefficient, because of its smaller bandgap, and a larger excitonic Bohr radius, which allows better modulation of its bandgap with size. For these reasons, Ge has been a widely-used material for CMOS-compatible PD fabrication.[1–4] Apart from its crystalline form, a variety of Ge nanostructures have been investigated for improved optoelectronic performance[4–10] including Ge QDs embedded in an oxide matrix for high-efficiency photodetection.[5,10–17] The principal advantages of Ge QDs include reduced phonon scattering, leading to longer carrier relaxation times, as well as confinement in all three spatial dimensions that can reduce the dark current, both contributing to higher SNR. Furthermore, Ge QDs are characterized by a tunable bandgap which allows broad wavelength selection, from the near-IR to the visible, and finally intersubband transitions are polarization independent in contrast to quantum wells. Typically, Ge photodetectors are operated at cryogenic temperatures in order to suppress the dark current, arising from thermally-generated carriers due to its smaller bandgap. In this work we have studied the temperature-dependent photoresponse and noise performance over the 100–300 K range in the visible and near-IR, of CMOS-compatible PDs based on Ge QDs embedded in an SiO_2 matrix as introduced in our previous work.[18]

S. Siontas, Dr. D. Li, Dr. P. Liu, S. Aujla, Prof. A. Zaslavsky, Prof. D. Pacifici
School of Engineering, Brown University, 184 Hope St., Providence, RI 02912, USA
E-mail: stylianos_siontas@brown.edu
Dr. P. Liu, Prof. A. Zaslavsky, Prof. D. Pacifici
Department of Physics, Brown University, 182 Hope St., Providence, RI 02912, USA

DOI: 10.1002/pssa.201700453

2. Fabrication Process

The photodetectors were fabricated by co-sputtering of Ge and SiO_2 targets on p^- (5–10 Ω cm) Si substrates held at a temperature of 400 °C yielding a 200 nm-thick oxide matrix with embedded Ge QDs.[18] Following deposition the samples were annealed at 500 °C in a N_2 environment for 30 min to generate larger size and higher density Ge QDs with improved crystalline quality.[18] Subsequently, an optically transparent, highly-conductive ~100 nm-thick indium tin oxide (ITO) layer was sputter-deposited as the top electrode. Photolithography was then performed to define several 1 mm^2 active area devices, obtained by etching away the ITO and Ge QD/SiO_2 layers using a dilute HF solution, with the aim of suppressing leakage current on the periphery as described in our previous work.[18] Subsequently, an indium back contact was used to attach the detector onto a 0.5 mm thick sapphire (Al_2O_3) substrate. The top and back electrodes of the photodetector were wire-bonded using

a 25 μm diameter Au wire onto a sample holder which was then mounted into a variable temperature closed cycle cryostat with fused silica windows for optical access.

3. Temperature-Dependent Photoresponse

The *I–V* characteristics of a 1 mm^2 active area photodetector were carried out in the dark and at a representative visible wavelength of 640 nm from 300 K down to 100 K with a 50 K temperature step. A continuous wave laser delivering constant optical power (P_{in}) of 12 μW, with a beam spot diameter of ~ 1 mm was used as an illumination source. All *I–V* measurements were carried out using a parameter analyzer with a measurement averaging time t_{avg} set to 1.6 s per data point. The mean and standard deviation of two consecutive measurements sets are presented in **Figure 1**(a), in which it can be seen that the standard deviation of the current, represented with error bars, is considerably small thus confirming robust devices with reproducible behavior. More specifically, the dark current decreases by approximately one order of magnitude for every 50 K of temperature reduction as a direct consequence of reduced thermal generation of electron-hole pairs. This, in turn, increases the rectification ratio at symmetric voltages of −2 and 2 V from four (at 300 K) to seven orders of magnitude (at 100 K). The photoresponse, presented in Figure 1(b), exhibits a considerable decrease at low and intermediate reverse voltages, which is attributed to weaker phonon-assisted tunneling at lower temperatures. However, the measured total current values at the preferred −10 V reverse bias converge to roughly the same value, leading to a far greater photocurrent/dark current ratio. The detector's photoresponse at −10 V as a function of temperature is summarized in the Arrhenius plot of **Figure 2**, also including the activation energy values estimated from the slopes of linear fits to the current curves. As extracted from Figure 2, at 300 K and −10 V of reverse bias the photodetector exhibits a spectral responsivity (R_{sp}) of 1.2 A W^{-1}, external quantum efficiency (EQE) of 226% and internal quantum efficiency (IQE) of 228% calculated for reflectance equal to 0.87% at 640 nm as presented in Ref. [18]. As previously reported,[16–18] the photoconductive gain mechanism responsible for EQE above 100% arises from the asymmetry in carrier transport: the much heavier tunneling mass of holes slows down their percolation through the Ge QDs, resulting in an effective positive charge in the QDs that favors the flow of the lighter electrons. These reported PD figures of merit are significantly higher than those of a conventional Si photodetector.[19] As for the 100 K case, despite the slight decrease in photocurrent, we still obtain values of $R_{sp} = 0.53$ A W^{-1}, EQE = 102%, and IQE = 103%. These values improve at lower illumination powers as shown in the following section, in which the detector's noise performance is studied as a function of operating temperature and incident optical power.

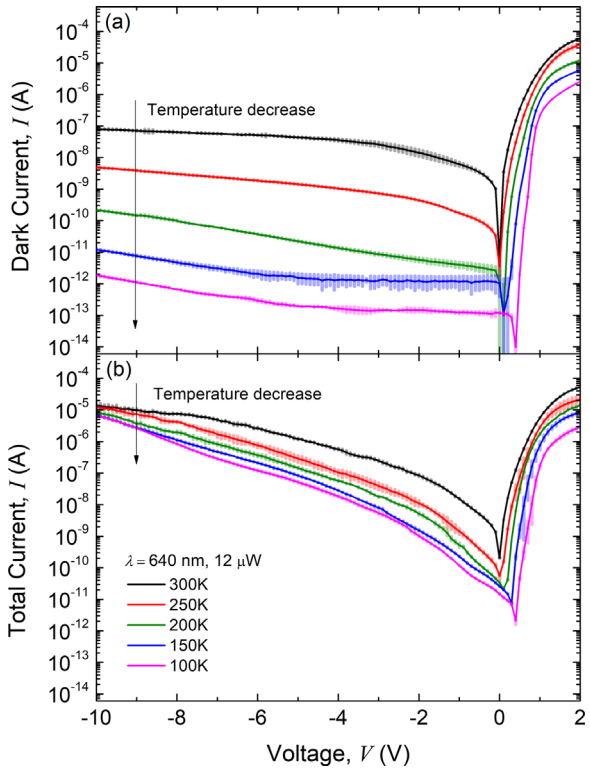

Figure 1. *I–V* curves versus temperature in the 100–300 K range of a 1 mm^2 photodetector (a) in the dark and (b) under illumination at 640 nm wavelength for 12 μW of incident power. Dark current decreases approximately one order of magnitude per 50 K as a consequence of reduced thermal generation of electron-hole pairs, whereas, the current under illumination slightly decreases as a result of suppressed phonon-assisted tunneling, stemming from decreased phonon densities at lower temperatures. The error bars represent the standard deviation from the mean of two consecutive measurement sets, confirming reproducible photodetector performance.

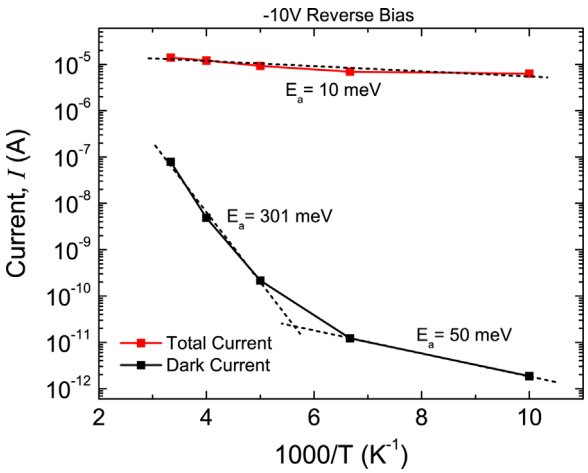

Figure 2. Arrhenius plots of current in the dark and under 640 nm illumination at 12 μW summarizing the photoresponse of the photodetector as a function of operating temperature at −10 V of reverse bias, presented together with activation energy values calculated from the slopes of linear fits to the current curves.

4. Temperature-Dependent Noise Performance

The noise performance of a photodetector is characterized by the signal-to-noise ratio (SNR) defined as $\mathrm{SNR} = I_{\mathrm{ph}}/\sigma_{\mathrm{n}}$, where I_{ph} is the photocurrent and σ_{n} is the total current noise. Two main sources of current noise must be considered, first being the photocurrent shot (Poisson) noise $\sigma_{\mathrm{ph}}^2 = 2e(I_{\mathrm{ph}}BG)$ associated with the discrete nature of photon-electron generation where e is the elementary charge, G is the internal gain (IQE) and B is the measurement bandwidth, that is, half of the reciprocal of the measurement averaging time as imposed by the Nyquist sampling theorem $B = (2t_{\mathrm{avg}})^{-1}$. The second source is the intrinsic thermal noise introduced by the detector circuit $\sigma_{\mathrm{th}}^2 = \left(\sigma_j^2 + \sigma_d^2\right)$ where $\sigma_j^2 = 4kTB/R$ is the Johnson-Nyquist noise introduced by the thermal motion of charge within the load resistance R connected in series to the PD, k is the Boltzmann constant and $\sigma_d^2 = 2e(I_{\mathrm{d}}BG)$ is the dark current shot noise.[19] The photocurrent and IQE dependence on various incident powers, ranging from 10 nW to 12 μW, were measured for operating temperatures of 300 and 100 K. The I–V curves for measurements carried out at the lowest and maximum values of the above optical power range are presented in **Figure 3**(a) and (b). At 12 μW of optical power, at −10 V of reverse bias, the current under illumination is approximately the same for both 300 and 100 K operation, as also evident in Figure 1(b). At 10 nW of incident power, for 100 K operation, the current is significantly lower than the 300 K case at low and intermediate voltages, however it exhibits a climbing trend as it approaches −10 V, attributed to the higher electric field, which lowers the tunneling barriers and mitigates the hopping process, finally leading to higher total current than at 300 K operation for the same −10 V bias. This, together with the greatly suppressed dark current at 100 K, suggests significantly higher photocurrent than that for 300 K operating temperature. In order to verify that this increase in total current is actually attributed to photocurrent and not to larger leakage occurring due to sample degradation, a second set of measurements was carried out. As seen in Figure 3 the very small standard deviation from the mean, represented by error bars, confirms that the device performance is unchanged as we recover the exact same current behavior in the dark and under illumination. Moving on, the photocurrent and IQE dependence on incident power including all intermediate values within the 10 nW to 12 μW range, is summarized in **Figure 4**(a) and (b) at −10 V of reverse bias. At operating temperature of 300 K, the photocurrent increases linearly with incident power and IQE remains approximately constant. On the other hand, at 100 K the photocurrent shows a much weaker sublinear power dependence, therefore leading to a magnifying difference compared to 300 K as incident power is lowered, see Figure 4(a). The mechanism

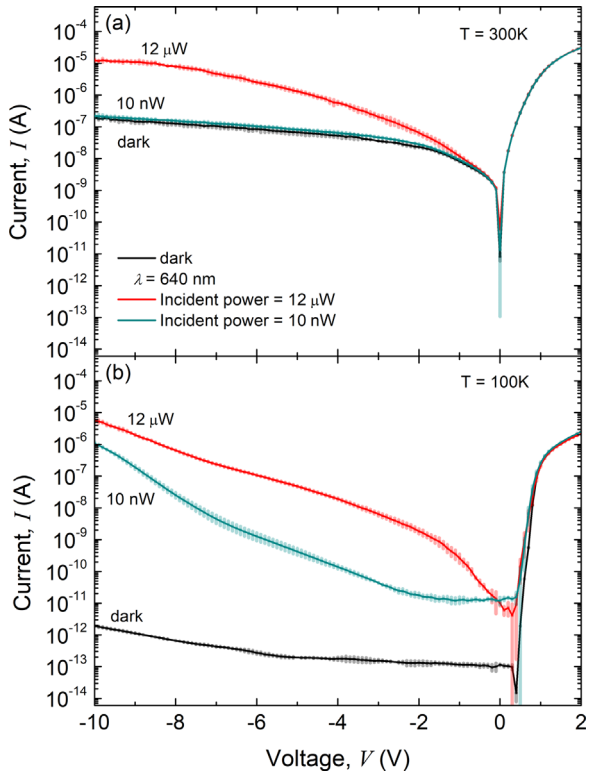

Figure 3. I–V curves in the dark and for 640 nm illumination at 10 nW and 12 μW of incident power, at operation temperatures of (a) 300 K and (b) 100 K. At 100 K the photocurrent for 10 nW of incident power exceeds that of 300 K operation, whereas at 12 μW they are approximately equal. The small standard deviation of two consecutive measurement sets, confirm robust detector performance by recovering same current in dark and under illumination after temperature and charging stresses.

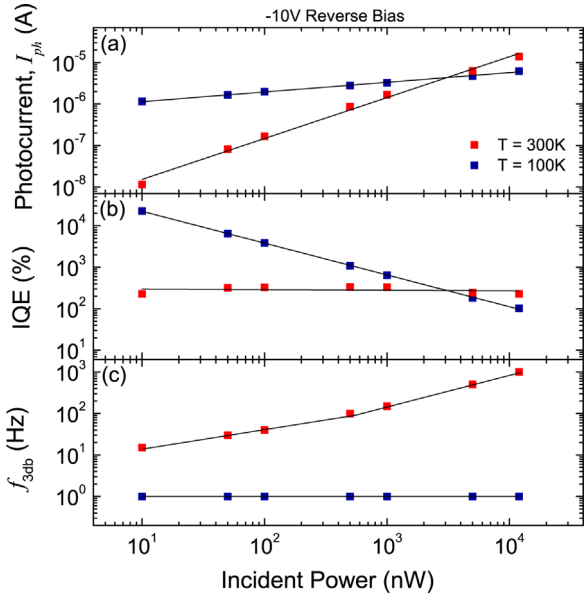

Figure 4. Experimentally measured dependence of (a) photocurrent, (b) IQE, and (c) 3 dB frequency response of the photodetector circuit on incident optical power ranging from 10 nW to 12 μW at −10 V reverse bias for operating temperatures of 300 and 100 K. At 300 K the photocurrent increases linearly with optical power, whereas at 100 K it exhibits a sublinear behavior resulting in higher IQE, due to longer hole lifetimes which also lead to a lower 3 dB frequency response at 100 K.

responsible for this trend is the following: At 100 K the number of available percolation paths within the QD layer through which electrons can tunnel reduces as a consequence of less available phonons to assist the hopping process, resulting in longer hole lifetimes. Therefore, the photocurrent tends to saturate at lower incident powers compared to 300 K as additional photo-generated electrons cannot tunnel through the QD layer because of the absence of additional available percolation paths (which would otherwise be thermally activated at higher temperatures). This saturating trend of the photocurrent and the longer trapped charge lifetimes lead to strongly enhanced IQE with values in excess of 22 000% as is shown in Figure 4(b). Additionally, the detector's circuit electrical 3 dB frequency response (f_{3dB}) was also measured via frequency-dependent roll off measurements of the voltage across the 15 kΩ load resistor using digital modulation of the laser[18] for both temperature cases. As seen in Figure 4(c), at 300 K the frequency response increases sublinearly with incident optical power, as the conductivity of the PD increases, leading to a smaller series resistance, thus a smaller RC time constant reaching a maximum of 1 kHz. This value agrees with our previous reported 3 dB bandwidth of 2 kHz for a 0.5 mm^2 area detector possessing a 50% smaller RC constant.[18] However, in the 100 K case, the frequency response is dramatically suppressed and remains around 1 Hz throughout the incident power range, an effect also attributed to the longer charge trapping and hopping times within the QD matrix.

Based on these findings, the two noise sources and SNR dependence on incident optical power for the 300 and 100 K operating temperatures are compared in **Figure 5**. As can be seen for 300 K there is a clear crossover from the thermally-dominated noise regime at low incident power, to the quantum regime dominated by the photocurrent shot noise at high incident power. The thermal noise σ_{th} dominates the low optical power range up to 700 nW at which point the photocurrent shot noise σ_{ph} takes over. When operating at 100 K the change in the carbon film load resistance R is negligible and so the thermal noise is lower by a factor of roughly three, because it is dominated by the Johnson noise in the load resistor (rather than the dark current term, which falls by several orders of magnitude). As for the total noise, at 12 μW it is approximately the same for both 300 and 100 K as it is dominated by the photocurrent shot noise which does not vary significantly at −10 V reverse bias. At 100 K, the total noise is observed to increase for diminishing incident power, and it is higher than at 300 K, as a result of significantly increasing photocurrent shot noise stemming from the greatly magnifying IQE up to 22000% as demonstrated in Figure 4(b). As a result, at 100 K the total noise is shot noise-limited over the entire power range. The above presented behavior of the photocurrent and photocurrent shot noise leads to higher SNR in the low-power regime of 10 nW, increasing from 2×10^4 at 300 K to 2×10^5 at 100 K, whereas the same maximum SNR of 7×10^6 is observed at 12 μW for both temperatures, as seen in **Figure 6**, an evidence that the photodetector benefits from 100 K operation only in the lower incident power regime.

The second important figure of merit to characterize the detector performance is the specific detectivity $D^* = (A)^{1/2}/\mathrm{NEP}$, where A is the photodetector area and NEP is the noise-equivalent-power normalized by the measurement bandwidth (B). NEP is a measure of the minimum optical power detectable by a photodetector, meaning that it is the power needed to generate a signal equal to the detector's intrinsic thermal noise floor σ_{th} resulting in SNR = 1, that is, $I_{ph} = \sigma_{th}$, for a measurement bandwidth B of 1 Hz, that is, a measurement time

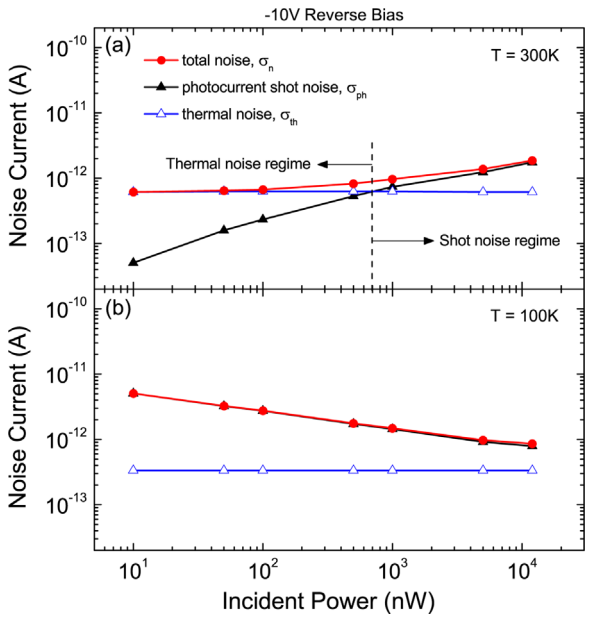

Figure 5. Calculated dependence of thermal noise, photocurrent shot noise, and total noise on incident power at operating temperatures of 300 (a) and 100 K (b) at −10 V of reverse bias. At 300 K there is a clear crossover at 700 nW between the thermal and shot noise-limited regimes, whereas at 100 K the noise is limited by the photocurrent shot noise over the entire power range, as the thermal noise is negligible (the total and shot noise curves overlap).

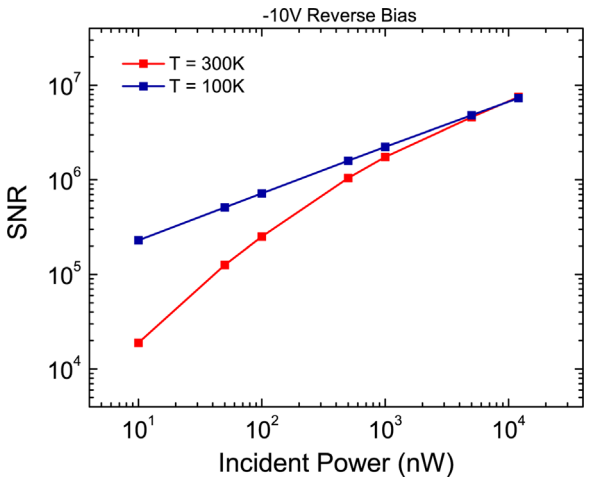

Figure 6. SNR dependence on incident optical power at reverse bias of −10 V for operating temperatures of 300 and 100 K, showing up to an order of magnitude improvement in the low-power regime at 10 nW when the PD is cooled to 100 K.

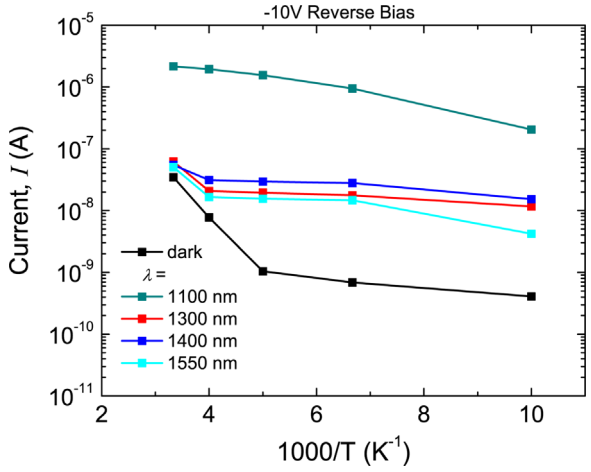

Figure 7. Arrhenius plot summarizing the temperature-dependent dark current and near infrared photoresponse at −10 V of reverse bias, showing photoresponse approximately equal to 3 orders of magnitude for 1100 nm and up to two orders of magnitude for the 1300–1550 nm range for temperatures below 200 K.

of 0.5 s. This implies that $\mathrm{NEP} = \sigma_{\mathrm{th}}/\left(R_{\mathrm{sp}} B^{-1/2}\right)$. Given that our measurements were carried out in a 1.6 s averaging time window ($B = 0.3$ Hz) this yielded $\mathrm{NEP} = 9.6 \times 10^{-13}\,\mathrm{W\,Hz^{-1/2}}$ and thus $D^* = 1.2 \times 10^{11}\,\mathrm{cm\,Hz^{1/2}W^{-1}}$ at 300 K, a value that is competitive or even superior to various other material photodetectors reported for a similar wavelength at 300 K in the literature.[20–27] Repeating the same procedure for the 100 K case yielded $\mathrm{NEP} = 5.3 \times 10^{-15}\,\mathrm{W\,Hz^{-1/2}}$ and thus $D^* = 2 \times 10^{13}\,\mathrm{cm\,Hz^{1/2}W^{-1}}$ which represents a two orders of magnitude improvement. It is important to note here that the specific detectivities reported above were calculated for spectral responsivity R_{sp} corresponding to the lowest incident optical power of 10 nW. This does not change the value of D^* for the 300 K case, where R_{sp} is approximately constant within the linear regime. But at 100 K R_{sp} increases dramatically in the low incident power regime as demonstrated in Figure 4(b), leading to a significantly lower NEP and thus greater D^*. The detectivity calculated for R_{sp} at the highest incident power of 12 μW is approximately the same for both 300 and 100 K cases, meaning that the detector's noise performance only benefits from operating at 100 K in the low incident optical power regime as is also evident in Figure 6.

Table 1. Summary of main figures of merit for various incident wavelengths at 300 K operation temperature.

Wavelength λ (nm)	P_{in}	R_{sp} (A W^{-1})	EQE (%)	IQE (%)	NEP (W Hz$^{-1/2}$)	D^* (cm Hz$^{1/2}$ W^{-1})
640	10 nW	1.2	225	227	9.6×10^{-13}	1.2×10^{11}
640	12 μW	1.2	226	228	9.6×10^{-13}	1.2×10^{11}
1100	12 μW	0.18	20	26.8	6×10^{-12}	1.7×10^{10}
1300	12 μW	0.002	0.22	0.25	4.7×10^{-10}	2.1×10^{8}
1400	12 μW	0.002	0.15	0.16	6.4×10^{-10}	1.6×10^{8}
1550	12 μW	0.001	0.11	0.11	8.1×10^{-10}	1.2×10^{8}

Table 2. Summary of main figures of merit for various incident wavelengths at 100 K operation temperature.

Wavelength λ (nm)	P_{in}	R_{sp} (A W^{-1})	EQE (%)	IQE (%)	NEP (W Hz$^{-1/2}$)	D^* (cm Hz$^{1/2}$ W^{-1})
640	10 nW	116	22475	22673	5.3×10^{-15}	2.0×10^{13}
640	12 μW	0.53	102	103	1.2×10^{-12}	9.0×10^{10}
1100	12 μW	0.017	1.92	2.60	3.6×10^{-11}	2.8×10^{9}
1300	12 μW	0.001	0.09	0.10	6.5×10^{-10}	1.5×10^{8}
1400	12 μW	0.001	0.11	0.12	4.9×10^{-10}	2.0×10^{8}
1550	12 μW	0.0003	0.03	0.03	1.9×10^{-9}	5.2×10^{7}

5. Near-IR Photoresponse and Noise Performance

Apart from visible excitation, the near-IR photoresponse of the Ge QD photodetectors was carried out in the 1100–1550 nm range. A super-continuum laser simultaneously outputting 800–2400 nm, with a ~1 mm diameter beam spot and narrow bandpass filters (FWHM ~ 10 nm) with center wavelengths of 1100, 1300, 1400, and 1550 nm intercepting the beam, to pick up the desired wavelength, were utilized to characterize the photoresponse of another 1 mm^2 Ge QD photodetector from the same fabrication batch. For wavelengths above 1100 nm, the Si substrate is practically transparent to incident light at 300 K, therefore only electron-hole excitation in the Ge QDs themselves can significantly contribute to the photocurrent. As a result, the photoresponse at near-IR excitation is considerably weaker. Nonetheless, as the temperature is lowered from 300 K, we do observe a photoresponse that is summarized in **Figure 7** (again, at −10 V reverse bias). While at 300 K the photoresponse in the near-IR is swamped by the dark current, cooling the PD below 200 K produces a photocurrent approximately three orders of magnitude higher than the dark current at 1100 nm and up to two orders of magnitude higher than the dark current in the 1300–1550 nm range. To summarize these findings, the main figures of merit characterizing the performance at 640 nm, as presented in the previous two sections, as well as for near-IR excitation are collected in Tables 1 and 2, for operating temperatures of 300 and 100 K respectively. We point out here that the reason why D^* shows reduced values at 100 K for near-IR wavelengths is because it has been calculated using responsivity measured at 12 μW and not in the lower optical power regime, where the device performance benefits from low-temperature operation as demonstrated previously.

6. Summary

To summarize, we have studied the operating temperature-dependent photoresponse and noise performance of Ge QD photodetectors in the 100–300 K range. The spectral responsivity and IQE obtained at 640 nm for 300 K operation are well above those of a Si photodiode, indicative of the internal photoconductive gain present in our devices. Cooling our detectors to 100 K determines an order of magnitude increase in SNR and two orders of magnitude improvement in specific detectivity (up

to $D^* = 2 \times 10^{13}\,\mathrm{cm\,Hz^{1/2}\,W^{-1}}$) at low incident optical power of 10 nW, due to photoconductive gain over 22 000% resulting from saturation of the QD charging process at low temperature. We also characterized the operation of our QD photodetectors in the near-IR range, 1300–1550 nm, where the Si substrate is transparent and only the Ge QDs contribute significantly to optical absorption, finding that the photodetectors are functional up to 1550 nm, as long as they are cooled to 200 K or lower temperature. To conclude, we have demonstrated Ge QD photodetectors that exhibit significant performance enhancement when operated at low temperature and incident power, and allow for extended near-IR wavelength detection capability in comparison to conventional silicon photodiodes.

Conflict of Interest

The authors declare no conflict of interest.

Acknowledgements

The authors would like to thank Zhi Jiang for the kind help during experiments. This work was supported by the National Science Foundation under grants DMR–1203186, CMMI–1530547, as well as Brown University seed award GR300030.

Keywords

germanium, near-infrared, photodetector, quantum dots, temperature

Received: June 30, 2017
Published online: October 4, 2017

[1] L. Chen, P. Dong, M. Lipson, *Opt. Express* **2008**, *16*, 11513.
[2] L. Tang, S. E. Kocabas, S. Latif, A. K. Okyay, D. S. Ly- Gagnon, K. C. Saraswat, D. A. B. Miller, *Nat. Photon*. **2008**, *2*, 226.
[3] V. Sorianello, A. De Iacovo, L. Colace, A. Fabbri, L. Tortora, E. Buffagni, G. Assanto, *Appl. Phys. Lett*. **2012**, *101*, 081101.
[4] M. Elkurdi, P. Boucaud, S. Sauvage, O. Kermarrec, Y. Campidelli, D. Bensahel, G. Saint-Girons, I. Sagnes, *Appl. Phys. Lett*. **2002**, *80*, 509.
[5] I. Stavarache, A. M. Lepadatu, T. Stoica, M. L. Ciurea, *Appl. Surf. Sci*. **2013**, *285, Part B*, 175.
[6] C. Y. Chien, W. T. Lai, Y. J. Chang, C. C. Wang, M. H. Kuo, P. W. Li, *Nanoscale* **2014**, *6*, 5303.
[7] X. Liu, X. Ji, M. Liu, N. Liu, Z. Tao, Q. Dai, L. Wei, C. Li, X. Zhang, B. Wang, *ACS Appl. Mater. Interfaces* **2015**, *7*, 2452.
[8] M. H. Kuo, W. T. Lai, T. M. Hsu, Y. C. Chen, C. W. Chang, W. H. Chang, P. W. Li, *Nanotechnology* **2015**, *26*, 055203.
[9] Y. Itoh, S. Hatakeyama, T. Kawashima, K. Washio, *Thin Solid Films* **2016**, *602*, 32.
[10] J. M. Shieh, Y. F. Lai, W. X. Ni, H. C. Kuo, C. Y. Fang, J. Y. Huang, C. L. Pan, *Appl. Phys. Lett*. **2007**, *90*, 051105.
[11] M. Fujii, O. Mamezaki, S. Hayashi, K. Yamamoto, *J. Appl. Phys*. **1998**, *83*, 1507.
[12] B. Zhang, S. Shrestha, M. A. Green, G. Conibeer, *Appl. Phys. Lett*. **2010**, *96*, 261901.
[13] S. Cosentino, S. Mirabella, M. Miritello, G. Nicotra, R. L. Savio, F. Simone, C. Spinella, A. Terrasi, *Nanoscale Res. Lett*. **2011**, *6*, 135.
[14] C. Palade, A. M. Lepadatu, I. Stavarache, V. Teodorescu, M. Ciurea, Semiconductor Conference (CAS), International (2013) pp. 31–34.
[15] S. Cosentino, E. Barbagiovanni, I. Crupi, M. Miritello, G. Nicotra, C. Spinella, D. Pacifici, S. Mirabella, A. Terrasi, *Sol. Energ. Mat. Sol. Cells* **2015**, *135*, 22.
[16] S. Cosentino, P. Liu, S. T. Le, S. Lee, D. Paine, A. Zaslavsky, D. Pacifici, S. Mirabella, M. Miritello, I. Crupi, A. Terrasi, *Appl. Phys. Lett*. **2011**, *98*, 221107.
[17] P. Liu, S. Cosentino, S. T. Le, S. Lee, D. Paine, A. Zaslavsky, D. Pacifici, S. Mirabella, M. Miritello, I. Crupi, A. Terrasi, *J. Appl. Phys*. **2012**, *112*, 083103.
[18] S. Siontas, P. Liu, A. Zaslavsky, D. Pacifici, *Appl. Phys. Lett*. **2016**, *109*, 053508.
[19] F. Träger (Ed.), *Handbook of Lasers and Optics*, Springer, Berlin Heidelberg **2012**.
[20] J. Yao, J. Shao, Y. Wang, Z. Zhao, G. Yang, *Nanoscale* **2015**, *7*, 12535.
[21] L. Dou, Y. M. Yang, J. You, Z. Hong, W. H. Chang, G. Li, Y. Yang, *Nat. Commun*. **2014**, *5*.
[22] J. Qi, L. Ni, D. Yang, X. Zhou, W. Qiao, M. Li, D. Ma, Z. Y. Wang, *J. Mater. Chem. C* **2014**, *2*, 2431.
[23] M. S. Choi, D. Qu, D. Lee, X. Liu, K. Watanabe, T. Taniguchi, W. J. Yoo, *ACS Nano* **2014**, *8*, 9332.
[24] D. S. Tsai, K. K. Liu, D. H. Lien, M. L. Tsai, C. F. Kang, C. A. Lin, L. J. Li, J. H. He, *ACS Nano* **2013**, *7*, 3905.
[25] Z. Liu, T. Luo, B. Liang, G. Chen, G. Yu, X. Xie, D. Chen, G. Shen, *Nano Res*. **2013**, *6*, 775.
[26] M. Sofos, J. Goldberger, D. A. Stone, J. E. Allen, Q. Ma, D. J. Herman, W. W. Tsai, L. J. Lauhon, S. I. Stupp, *Nat. Mater*. **2009**, *8*, 68.
[27] M. Razeghi, A. Rogalski, *J. Appl. Phys*. **1996**, *79*, 7433.